EUROPEAN ORGANIZATION FOR NUCLEAR RESEARCH
European Laboratory for Particle Physics

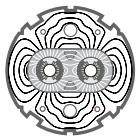

Large Hadron Collider Project **LHC Project Report 1007**

GEOMETRICAL TOLERANCES FOR THE QUALIFICATION OF LHC MAGNETS

J.B. Jeanneret, AB/ABP

Abstract

This report presents a detailed summary of all the geometrical tolerances which were defined in order to qualify the LHC magnet assemblies for aperture.

Administrative Secretariat
LHC Division
CERN
CH-1211 Geneva 23
Switzerland

Geneva, June 2007

Contents

List of Tables

List of Figures

1 Introduction

The mechanical aperture of most LHC magnets was made quite small for cost and performance considerations. It was therefore necessary to impose quite strict geometrical tolerances in order to ensure an adequate normalised aperture for beams. In many cases conflicting requirements between construction and beam aperture required to both define slot-dependent tolerances and make sorting. There are many families of magnets, each of these requiring dedicated tolerances definitions. In this report, the overall approach used to build-up tolerances is discussed in Sections 2. Detailed definitions of tolerances for each species of magnet assemblies are presented in Section 3 to 13. In each section, references to codes and files that helps the qualification process will be listed together with their locations. Finally, a few difficult cases are presented in Section 14.

The main aim of this report is to provide a complete summary of tolerances in order to help the process of later replacement of magnets. We therefore discuss only marginally all the work done in collaboration with the magnet builders in order to comply with the aperture needs. This is presented in many notes and report of the LHC report and note series which can be found via the LHC web home page [1]

2 Overall framework

The method used to define tolerances was chosen in order to allow for minimising at best the interference between the different activities and elements which contribute to the geometrical errors of LHC magnet assemblies. The identification and the quantification of error sources which impact on the tolerance budget for LHC magnet assemblies were separated into homogeneous components which were worked-out one-by-one. The summing-up of all the components was then compared to the beam requirements. An iterative work was then performed in order to get a coherent set of tolerances for every magnet families. This historical process will not be further discussed. We will concentrate on the resulting specifications, expressed as data set of tolerances which must be satisfied at several step of the life of an element, from fabrication of the cold mass to installation then beam operation in the tunnel.

2.1 Reference system

The reference system chosen is given in Figure 1. The x coordinate is horizontal pointing towards the ring center, the z one is vertical and y is along the beam line, pointing forward with the clockwise Beam 1.

2.2 Beam and optics

The method used to compute and specify the space needed to house the beam is described in Chapter 4.3 of [2]. The transverse beam size proper is quantified with the normalised primary aperture n_1 expressed in 2D r.m.s. transverse beam size units. The net primary aperture of every element in the LHC ring must satisfy the specification

$$\begin{aligned} n_1 &= 7.0 \text{ in MB} \\ n_1 &= 7.0 \text{ in QF} \\ n_1 &= 6.7 \text{ in QD} \end{aligned} \tag{1}$$

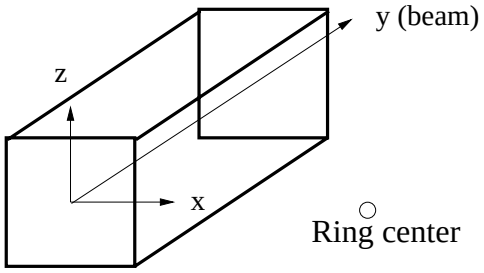

Figure 1: The reference system which complies with the definitions of the survey team.

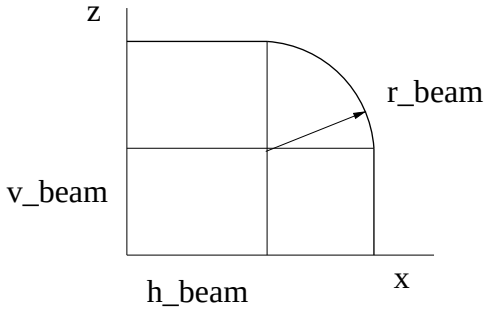

Figure 2: The generic 2D double racetrack area used to define the geometrical tolerances of the beam elements in the MadX optics code.

$$n_1 = 7.0 \text{ in all other elements}$$

where MB stand for Main Dipole, QF for focussing quadrupoles and QD for defocussing quadrupoles. With this specification, the secondary halo, and therefore the overall betatronic beam aperture is $A_{\text{radial}} = 1.4 \times n_1 = 10$ at 45° and $A_{\text{x,z}} = 1.2 \times n_1 = 8.4$ at 0° and 90°, including a budget for beta-beating. The overall transverse space occupied by the beam must be made larger in order to house displacements by dispersion and closed orbit errors. The latter contribution is for most of it related to quadrupole transverse displacements and b_1 errors in MB's. But this effect is non-local, e.g. the kick induced by a quadrupole displacement is converted to a beam displacement at some distance. The closed orbit is for most of it corrected in the control room and therefore nearly uncorrelated locally from magnet displacement. The closed orbit thus appears in the beam tolerance budget (see Table 4.6 p. 70 of [2]) and is separated from the magnet misalignment error, which reduces the available aperture locally, see Section 2.4. In practice, the aperture is computed using the APERTURE module [3] of the MadX optics code [4]. All the beam parameters are fixed by default to the LHC nominal values for the worst case of injection and collision conditions. On the other hand, the mechanical tolerance are specified element by element with a set of three parameters $(r_{\text{beam}}, h_{\text{beam}}, v_{\text{beam}})$ which define a double race-track tolerance area, see Fig. 2, together with aperture definitions.

2.3 Magnet assemblies and geometrical data

2.3.1 Cold elements

The cold elements are measured with a laser-based Leica system all through their two cold bores after being installed in their cryostat enveloppe and cold tested [5]. In

addition, several reference points and flange axis are measured. The reference system is defined through a fit of the best plane minimising the residuals of the two profiles for two cold-bore elements. A best central axis is also fit in this plane. For single bore elements, the best fit is constrained such as to keep the magnetic vertical axis being straight-up. All the measured data are finally expressed in this referential, including the external survey targets. The profile data are then re-expressed as their difference to the theoretical cold bore axis. The final data set, called WP08 for the Main Dipole and WP18 for all the other cold magnet assemblies is used to qualify the magnet. Further measurements are made after installation of the beam screens (WP09/WP19), but only at the extremities. These data are used mostly to check the stability of the assemblies. The WP08/WP18 package is therefore the central data set used to check the tolerance conformity.

2.3.2 Warm elements

As for warm magnets, the vacuum chamber is centered closely to its theoretical position at its extremities with respect to the central axis of the iron yoke. The positioning error was calculated then checked in-situ. The measured default of rectitude of the yoke was added to the error. The longitudinal profile of the vacuum tube was not measured once installed. But whenever the chamber is not constrained inside the yoke (e.g. large aperture dipoles, or loose space inside quadrupoles), the rectitude of the bare chamber was measured, and added as an error. The resulting figure of merit was either used to define the tolerance of the element (as an offer to be compared to the needed tolerance) or, if necessary, sorting was made such as to comply to pre-defined tolerances.

2.4 Tolerance split-down

Whenever there are numerous contributions to a tolerance budget, two extreme methods can be used, namely linear or quadratic addition of each contributions. The latter case is justifiedonly if all contributions add randomly. This was found too dangerous, partly because some work steps were to occur after the tolerance budget was fixed and therefore no margin was left in case of bad surprises. In addition, the interferences between very different activities were found to be counter-productive in a context of tight planning. On the other hand, linear addition resulted in a tolerance budget which proved to be unaffordable, because many fundamental parameters were fixed since long and could not be changed, in particular the coil inner diameters. A compromise was found by splitting the budget between clearly separated group of contributions, which are added linearly. Then inside each group, quadratic addition is used.

As for cold magnets, three groups were defined, namely beam screen, cryostat assembly and finally all together dynamic movements, survey error and tunnel movements. The sum of the three contributions is called *beam* tolerances below.

2.4.1 beam screen

Once equipped with its sliding supports, the beam screen clearance w.r.t. to the cold bore was ≈ 1 mm, in order to allow it to be introduced safely. This fixes its overall maximum misplacement w.r.t. the cold bore. This misplacement was subtracted from the mechanical neat inner radius, thus defining a neat beam screen aperture, which is the quantity reported in the MadX LHC sequence and in Table 1. The beam screen tolerance

Table 1: Beam screen sizes as used for aperture calculations with MadX, once the maximum excursions of the screen inside the cold bore are deduced form the mechanical inner sizes.

Parent cold bore	radius R[mm]	Half-flat opening H or V [mm]	Parent element
50A	22.0	17.15	MB,MQ, MQM@1.9K
50L	22.6	17.7	MQM@4K
53	22.9	19.0	MQXA.1
63	29.0	24.0	MQXB, MQXA.3, MQY, DFBA
69	31.3	26.4	MBRC
74	33.7	28.8	MBX, DFBX

Table 2: Contribution of dynamic movements, survey error and tunnel movements gathered together under the label *tunnel*.

Element	Δx_{tunnel} [mm]	Δz_{tunnel} [mm]	Δr_{tunnel} [mm]
MB	0.6	0.0	1.0
MQX	0.0	0.0	0.6
MQ,MQM,MQY,D,DFB,Warm magnets, MBX,MBRC,MBRB,MBRS	0.36	0.0	0.84

does not appear any further explicitly in the tolerance break-down. All the other useful data concerning the beam screen and its orientation in every element can be found in [6] and [7].

2.4.2 Dynamic movements, survey error and tunnel movements

Survey errors and tunnel movement can be safely deduced from LEP experience. The tolerances for LHC are built-up by considering that the ring will be re-aligned every year, in order to miminise the contribution of tunnel to a reasonably achievable minimum. More precisely, it is foreseen to re-align every element vertically, and to check their tilt and correct if necessary. An overall radial tolerance budget $\Delta r_{\text{tunnel}} = 0.84$ mm was determined for cold mass dynamic deformation, survey error and tunnel movements (slightly increased values are used for the main dipole to cope with cold mass stability issues, see below). In the horizontal plane, the tunnel is considered to be stable enough such as to avoid visible displacements in the range of ~ 0.1 mm over periods much larger than a year [8]. The largest contribution to horizontal displacement are induced by a tilt of the tunnel floor which, with the height of the beam axis being $\Delta z = 890$ mm can be quite large. As a result, the horizontal tolerance must be larger than the vertical one. Depending on the family of assemblies, this difference may change a bit because of different level arm effects between the feet and the extremities of the assemblies, but we took it constant for all elements as $\Delta x_{\text{tunnel}} = 0.36$ mm, except for the MB for which $\Delta x_{\text{tunnel}} = 0.6$ [10]. The budget for this contributions is called *tunnel* in Table 2.

2.4.3 *Stability issues*

In order to check that the tolerance budget beyond WP08/18 is indeed realistic, a systematic campaign of verification of the cold mass stability inside its cryostat was performed together with the survey team. After being fiducialized, most of the dipoles were stored for a long time (in some cases nearly for 2 years) and far away from the SMA18 building. Then, they were transported to the SMI2 building were the beam screen was inserted. After this step, a control cartography was performed (WP09), where the survey targets, the reference marks on the extremities of the cold mass and the flange positions were measured with the same Leica system used at WP08. Then, by mapping the survey targets of the two packages WP08 and WP09, we get both the relative position of the reference marks, and eventual deformations of the cryostat enveloppe on which the survey targets are fixed. We found ∼25 MB's which exhibited deformations above 0.5 mm mostly in the horizontal plane. These cases were inspected one-by-one and the deformations could all be explained. Most of them suffered target damage and few cases were subject to delayed further cartography. The first set was repaired and the reference fiducialisation is now WP09 for these elements. The latter could be explained by transient deformation due to sudden temperature changes which induce a temperature gradient of the cryostat enveloppe or of the cold mass. Similar effects were observed whenever a fiducialisation was made too rapidly after a cold test. The delayed cartography was in some cases repeated once more in the tunnel and the assemblies were always found stable inside < 0.5 mm w.r.t. a budget of 1.05 mm, thus leaving margin for ageing deformations. It can be concluded that the tolerance budget quoted in Section 2.4.2 is indeed realistic. In turn, this indicates that the choice of qualifying the assemblies at the step WP08/18 is an adequate choice.

2.4.4 *Cryostat assembly*

Once beam aperture requirements, beam screen tolerances (Section 2.4.1) and tunnel (Section 2.4.2) contributions are set, the tolerances for cryostat assembly are obtained by subtraction as follows

$$\begin{aligned} h_{\mathrm{WP08,WP18}} &= h_{\mathrm{beam}} - h_{\mathrm{tunnel}} \\ v_{\mathrm{WP08,WP18}} &= v_{\mathrm{beam}} - v_{\mathrm{tunnel}} \\ r_{\mathrm{WP08,WP18}} &= r_{\mathrm{beam}} - r_{\mathrm{tunnel}} \end{aligned} \tag{2}$$

In other words, with the other components being reduced at the minimum level, the geometry of the cryostat assembly must comply with what remains. In order to match the offer and the demand, several steps were introduced in order to get more flexibility for the fabrication of the cold masses and for cryostating. In particular, as explained in Section 2.3.1, the fiducialisation is made relative to a best fit of the cold bore profiles. This prevents all the macroscopic geometrical errors of the cold mass and the cryostat imperfections to contribute to the tolerance budget. Then, whenever it is necessary and possible, geometrical sorting is performed, see in particular the case of the main dipole in Section 3. Finally, if necessary a small transverse shift can be applied in order to bring an element back into tolerance. These shifts, defined with horizontal, vertical and tilt components are loaded in a database together with the reference fiducialisation package WP08x, with x the selected package whenever there more than one was performed. The survey team uses these set of data when aligning the element in the tunnel.

Table 3: Silver Tolerances for the main dipole, as split between the magnet proper at fiducialisation (A), its potential later dynamic deformation (B), the alignment error and tunnel movement over one year (C), D the quadratic sum of B and C, and the displacement of the cold bore of the magnet as seen by the beam (E). All data in mm.

Plane	WP08	MB dynamic	Tunnel	$\sqrt{B^2+C^2}$	Beam
Column	A	B	C	D	E
Horizontal Δx	1.15	1.05	1.2	1.6	2.75
Vertical Δz	0.65	0.45	0.9	1.0	1.65

Table 4: Silver racetrack tolerance data for the Main Dipole at the time of fiducialisation (WP08) and in the tunnel after one year of operation, as deduced from Table 3.

Step	h [mm]	v [mm]	r [mm]
WP08	0.5	0	0.65
Tunnel	0.6	0	1.0
Beam	1.1	0	1.65

2.4.5 Overall results

The qualified elements belong to one of the following cases :

- Specified tolerances stricktly met or exceeded.
- Specified tolerances marginally missed. In this category, the condition (1) was missing $\delta n_1 \sim 0.1$. The latter default, which corresponds to a lack of space $\delta x < 0.2$ mm must be compared for exemple to the closed orbit budget $CO_{\rm radial} = 4$ mm. It can therefore easily be compensated locally if necessary.
- Specified tolerances missed by $\delta n_1 > 0.1$. These cases are discussed in detail in Section 14.

3 Main Dipole

The split-down of the geometrical tolerances for the main dipole can be found in Ref. [10] for the so-called 'Silver magnets' (S) which can be installed in any arc location proper, i.e. excluded the Dispersion Suppressor part which are located at the end of the arcs between Q7 and Q13. The data are summarized in Tables 3 and 4. The beam screen of the arc magnets is circular with flat part on the top and bottom sides, in order to house its cooling capillaries. The tolerance requirement was found to be more demanding in the vertical plane. The resulting race-track tolerance was thus defined with a vertical component $v_{\rm MB} = 0$. It is depicted in Figure 3.

3.1 MB sorting

The tolerances at WP08 are quite severe, as shown in Table 4 and Figure 3, of the order of $\Delta x_{\rm WP08} < h_{\rm WP08} + r_{\rm WP08} = 1.15$ mm and $\Delta z = 0.65$ mm. In the horizontal plane, in spite of the decision made to block transversely the central cold foot of the cold mass in the cryostat [9], the horizontal excursion of the profile are often beyond $\Delta x_{\rm WP08}$, even if the cryostated cold mass appeared to be much better and much stable

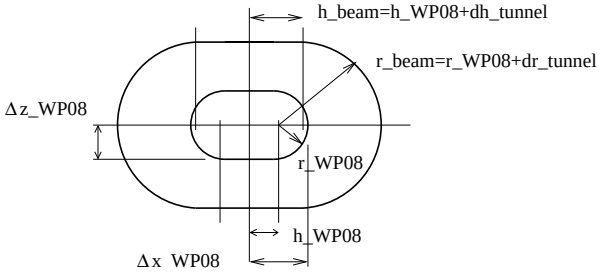

Figure 3: Racetrack 2D-tolerance for the main dipole, both at fiducialisation (WP08) and as seen by the beam on its central trajectory.

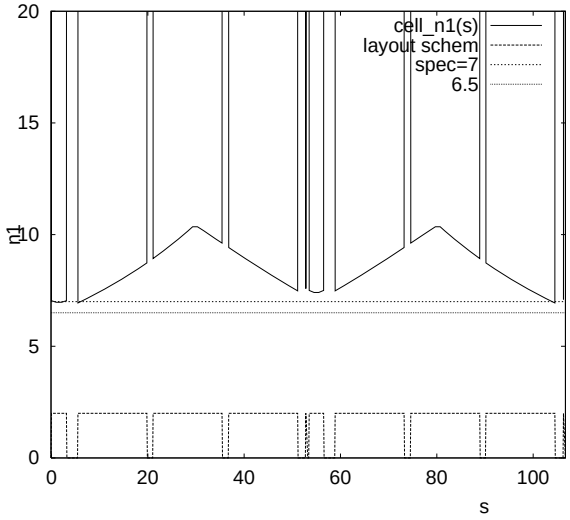

Figure 4: Primary aperture n_1 in arc cells, as computed with Silver tolerances. From left to right, the elements are a horizontally de-focusing quadrupole, 3 main dipoles, a horizontally focusing quadrupole then again 3 MB's. The MB which is located at the left of a group of three is said to be in a LEFT position (L), the central one in a MID-cell position (MC) and the last one is in a RIGHT position (R).

Table 5: The tolerance data for the geometry classes of the Main Dipole at WP08. The parent classes are Silver (S) and Golden (G). Their daughter classes apply to specific positions of a MB into an arc half-cell location, see text. All data in mm.

		Connection side			*Lyra side*		
Parameter		h	v	r	h	v	r
Class							
Golden	G	0.8	0.5	0	0.8	0.5	0
Golden Left	GL	0.8	0.5	0	0.8	1.5	0
Golden Right	GR	0.8	1.5	0	0.8	0.5	0
Parameter		h	v	r	h	v	r
Class							
Silver	S	0.5	0	0.65	0.5	0	0.65
Silver Left	SL	0.5	0	0.65	0.5	0	2.00
Silver Right	SR	0.5	0	2.00	0.5	0	0.65
Mid-Cell	MC	0.5	0	3.00	0.5	0	3.00

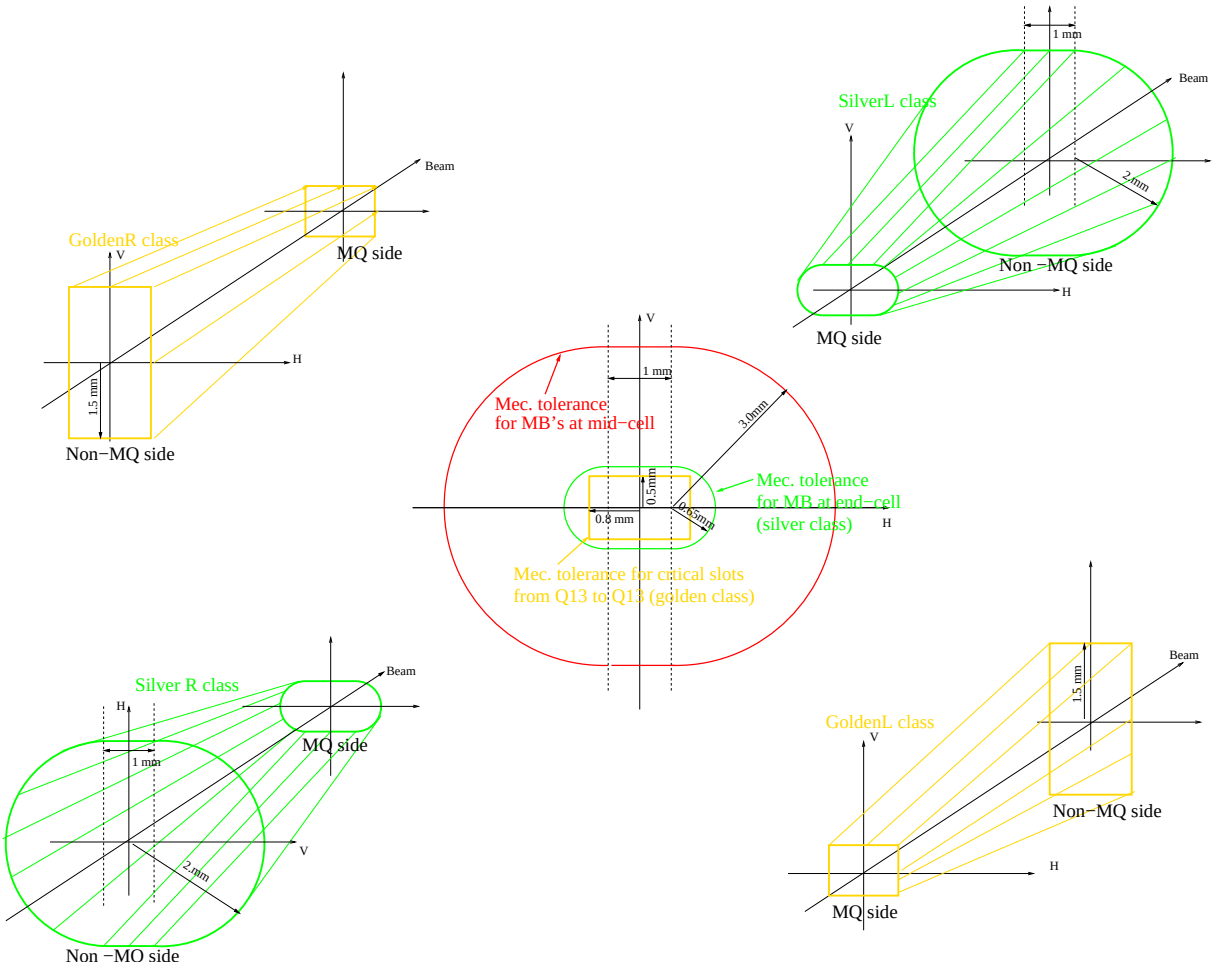

Figure 5: Geometry classes of the main dipole at WP08. Courtesy of S. Fartoukh.

with this option. In the vertical plane, the gravitional sag in between the three cold feet and at the extremities has a peak-to-peak amplitude of $\Delta s_v = 0.35$ mm. The margin left to the other contributions is very small. It was therefore proposed to do a geometrical sorting of the magnets [11, 12, 13]. The normalised aperture at constant tolerances is varying substantially along an arc-cell, as shown in Figure 4. The tolerances of Table 4 are adjusted to ensure that $n_1 = 7$ at the most demanding locations, which is near a QD. This set is called 'Silver' and a MB satisfying these tolerances is called 'Silver' or S-MB with respect to geometry. The Figure 4 shows that the central mid-cell magnet allows for a larger tolerance (MC tolerances and MC-MB). A MB located at the left of a mid-cell can have a relaxed geometry on its downstream side, and must be 'Silver' only at its upstream or left side. A magnet satisfying these criteria is called 'Silver Left' or SL. Conversely a magnet which is 'S' only on its downstream or right side is called SR. The tolerance of a SL or SR magnet is a racetrack which is Silver at one extremity and for which r grows linearly along the cold mass with

$$r(s) = r(0) + [r(L) - r(0)]s \quad \text{with} \quad \mathrm{s} = [0, \mathrm{L}] \ , \tag{3}$$

with L the cold mass length and $r(0)$ and $r(L)$ taken from Table 5.

In the dispersion suppressors, the optics is slightly altered and some location require tolerances which are even smaller than Silver ones. It was proposed to define 'Golden' tolerances for these locations [12, 13]. Similarly to the Silver case, GL and GR geometry classes were defined. Golden parameters are given in Table 5. 3D-views of all the classes are shown in Figure 5.

This is quite a complicated classification, but it was made necessary in order to offer enough sorting flexibility, because the magnet must also be sorted magnetically for their transfer functions, their a_2 and b_3 random multipolar error [12]. And with the aid of dedicated computer codes, the classification is made simple to use.

3.2 Codes for MB aperture and tolerance

Data retrieval and plotting of WP08 fiducialisation for MB's can be made with Unix Perl scripts which access Oracle. In addition, shifts can be applied in order to adjust a cold mass. As well, the slot of a MB can be retrieved and a comparison between WP08 and WP09 can be obtained. Codes are stored at

`/afs/cern.ch/eng/lhc/aperture/mbqualif/`
Using:

`wpack [mb|file1] [def|file2] [plot|no]` ,
with 'mb' a MB serial number, provides a summary at the terminal, summary table files (classes, fiducialisation history) and two plot files per MB (e.g. if MB serial number is 2388:
`mb2388-ITP20.ps and mb2388-WP08x.ps .`
WP08x is the latest WP08 performed. ITP20 is the profile as measured at the factory. Alternatively to a single MB number, a filename 'file1' can be provided which contains one MB number per line. 'def' points to a default tolerance table
`/afs/cern.ch/eng/lhc/aperture/mbqualif/tol_mb_wp08`.
The user can supply his own file as 'file2'. With the option 'plot', the plots are printed automatically. Whenever shifts must be applied, or if another package than the reference

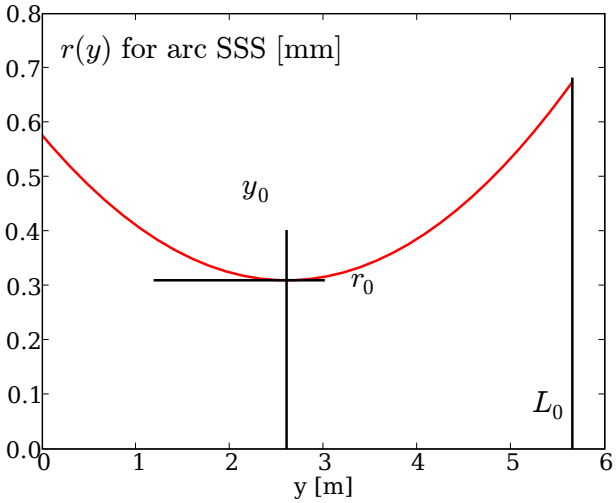

Figure 6: The running racetrack parameter $r(y)$ of the arc SSS assemblies.

need be analysed, use :

`mbgeo mb fidu def dx dz`
Automatic print of the .ps is provided by default. The slot allocated to MB is obtained with

`getslot mb`
A comparison WP08/WP09 is obtained with :

`w9one mb`
The result is a file named 'WP09-WELD_mb'.

While for an arc slot it is enough to identify a MB of at least class SL or SR, a slot in the dispersion suppressor requires more work. Two MadX runs must be made with a set of tolerances for each extremity of the slot.

4 Connection cryostats at Q11

In every dispersion suppressor, there is a missing dipole on the IP-side of Q11. This space is occupied by a Connection Cryostat (with layout name LE) which is basically an empty cryostat which ensures the continuity of helium lines and electrical bus-bars. For being located next to a quadrupole in the Dispersion Suppressor, its geometry must be 'Golden Left' on the L-side of an insertion and Golden-Right on the R-side. See Table 5 for GL and GR tolerances.

5 Short Strait Sections in the arcs

In the Short Strait Sections (SSS), the beam size reaches its maximum at the center of the main quadrupole (MQ). One aperture is focussing and the other one is defocussing. The adjustment of the geometry of the SSS is first made globally. The tolerances are therefore fixed by considering the maximum beam sizes in both apertures. Only during the qualification process, small transverse tilts can be applied to optimize the aperture in

Table 6: Racetrack tolerance data for the main quadrupole at the time of fiducialisation (WP18) and for the beam after one year of operation.The latter is the sum of the contribution WP18 and tunnel.

Step	h [mm]	v [mm]	r_0 [mm]	a[mm $\times$ m^{-2}]
WP18	0.54	0	0.30	3.92 10^{-2}
Tunnel	0.36	0	0.84	3.92 10^{-2}
Beam	0.90	0	1.14	3.92 10^{-2}

one bore while not degrading it in the other bore. The adjusted tolerances at fiducialisation of the SSS (WP18) are quite small, see Table 6, i.e. $\Delta x_{\rm WP18} = h_{\rm WP18} + r_{0,\rm WP18} = 0.84$ mm and $\Delta x_{\rm WP18} = 0.3$ mm. Even by relaxing a bit on beam aperture, by accepting that in the QD aperture, the condition (1), $n_1 = 7$, becomes

$$(n_{1,\rm QF}, n_{1,\rm QD}) = (7.0, 6.7) \ , \tag{4}$$

in order to avoid a null vertical tolerance at WP18. In order to add some flexibility, we made use of the decreasing beam size and dipersion away of the MQ center, and allowed the radial component r of the race-track to grow quadratically around the MQ center, such as to fit with the constraint Equation (4) all along the SSS. The resulting running $r(y)$ at WP18 is

$$r_{\rm WP18}(y) = r_0 + a(y - y_0)^2 \text{ with } y_0 \text{ the MQ center} \ , \tag{5}$$

with r, r_0 in mm and y, y_0 in m. It is displayed in Figure 6. The quantities r_0 and a are given in Table 6. The reduction from tunnel (or beam) tolerances down to WP18 ones is explained in [14].

6 Special Short Strait Sections in the dispersion suppressors and matching section elements

The optics function in the quadrupoles assemblies of the dispersion suppressors and of the matching sections (SpSSS) do not have the regularity of the arcs. Therefore the geometrical tolerances must be defined on a one-by-one basis and in most cases they must be made variable along the assembly. To simplify the qualification work, we used a generic approach for the tolerances. A racetrack tolerance is defined for the beam/tunnel such as to devote the radial r part to the tolerances beyond WP18 only ('tunnel') and to subtract a budget for tilt effect on the horizontal plane. We use the tunnel data of the MQ, see Table 6 and also Table 2 in Section 2.4.2. This is depicted in Figure 7. We therefore defined a rectangular tolerance area at WP18, with $h_{\rm WP18} = 0.9$ mm and $v_{\rm WP18} = 0.6$ mm. With this, more than 70% of the assemblies fit with the condition (1). In the remaining 30%, a fair fraction exhibited a geometry better than the above generic tolerance and allowed to recover the condition (1). A few difficult cases are discussed one-by-one in Section 14.

In order to help for the qualification work, a code allows to get a map of tolerances for any SpSSS on a one-by-one basis using the LHC MadX sequence [15] to adjust to the condition (4).
This code is found as

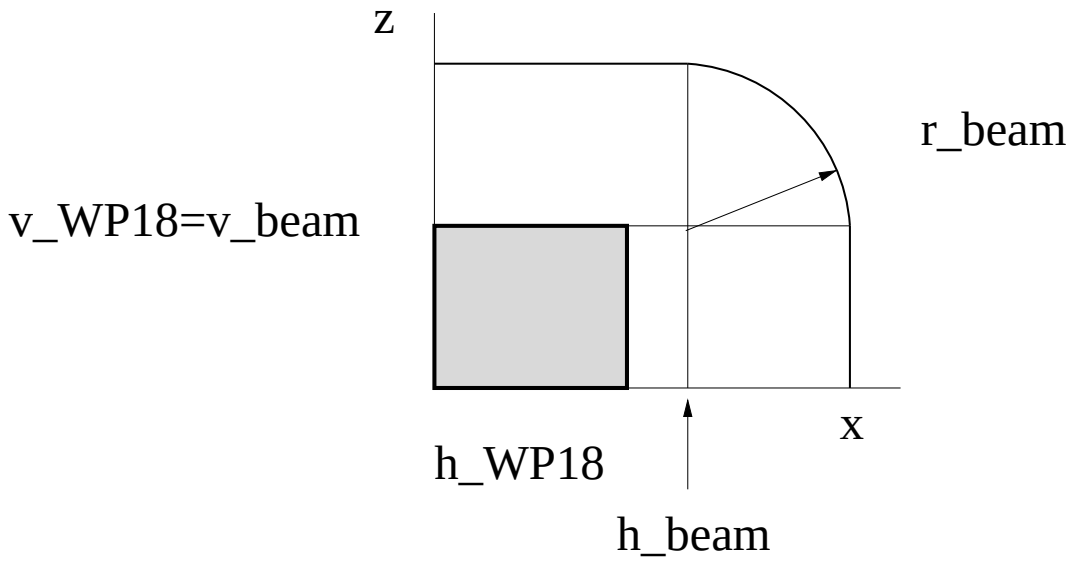

Figure 7: Tolerances for the SpSSS at WP18 and for the beam.

`/afs/cern.ch/eng/lhc/aperture/madx_ap/s4n1.pl`
The usage is
`s4n1.pl elem`
or
`s4n1.pl elem tolh`
with *elem* given as QnLm or QnRm , e.g. Q10L5. The horizontal tolerance is fixed by default to $h = 0.9$ mm. Another value can be chosen by providing the quantity *tolh* in the command line. The result is a table file called n1.elem. It provides n_1 along the assembly for a series of *tolv* values.

7 Cold feed-boxes of the arcs : DFBA

The DFBA elements are located at the extremity of the dispersion suppressors on their IP-side. They house two cold bores in continuity with the dispersion suppressor. Their design being quite late, it was decided to make use of large cold bores to avoid surprises related to geometry, see *DFBA* in Table 1. Thanks to this choice, an aperture $n_1 > 8$ is granted with tolerances as large as $h = 4$ mm and $v = 3$ mm. For a further split between flange data as measured (Workshop) and a budget for possible lack of rectitude of the cold bore which is not measured on the assembly, see Table 7 and [16] for some details. As of the writing, nine out of sixteen DFBA are measured and comply with these tolerances [16].

8 Triplet assemblies in experimental insertions

The beam space occupancy in the triplet quadrupoles is governed by the β^*, the crossing angle $\alpha_{\rm cross}$ and the parallel separation $d_{\rm IP}$ at the crossing point. These value are taken from the Design Report [2], see Section 4.2, p. 47 and Tables 4.2/4.5 therein. The beta functions and the crossing angles were slightly modified after the release of [2] in

Table 7: Tolerances for the DFBA.

Step	h [mm]	v [mm]	r [mm]
Workshop	3.0	2.0	0.0
Rectitude	1.0	1.0	0.0
Tunnel	0.36	0.0	0.84
Beam	4.36	3.0	0.84

some cases. The values used here are listed in Table 8. The tolerances for the single bore triplet quadrupoles assemblies are adjusted in order to get $n_1 = 7$ for the worst case of Beam 1 and Beam 2 and for the worst of the three following cases [17]

INJECTION We used the new value $\beta^* = 17$ m (formely 18 m) at point IR1 and IR5. The functions $n_1(s)$ are displayed in the first two rows of Figure 8. We notice that the aperture is more limited in IR2 and IR8 with tolerances which are identical in the 4 insertions, see sub-plots 13, 14, 23 and 24 in Figure 8. It was therefore proposed to move slightly the IP transversely in IR2 and IR8in the crossing plane in order make symmetric the crossing trajectories of the two beams at the center of Q2. This way we can enlarge the tolerances in IR2 and IR8 at injection and improve the sorting flexibility if necessary.

PRE-COLLISION NOMINAL Here, constraints appear only in IR1 and IR5. IR2 and IR8 are weekly squeezed ($\beta^* = 10$ m as for injection), see Table 8 and thus do not export much parasitic dispersion in IR1 and IR5. Tolerances are fixed with this configuration in IR1 and IR5.

PRE-COLLISION WORST CASE This extreme condition corresponds to an hypothetical and much unlikely case where the four insertions are squeezed, see Table 8. In practice, IR2 will be squeezed to $\beta^* = 0.5$ m only in ion operation, therefore with a quite smaller crossing angle of $\alpha_{\rm cross} = 80$ μrad. In IR8, the quoted value $\alpha_{\rm cross} = 210$ μrad is not coherent with $\beta^* = 1.0$ m, it shall be at most $\alpha_{\rm cross} = 155$ μrad in order to satisfy aperture constraints. The need for low-beta is foreseen only for operation with low intensity beams in the early days, in which case a reduced crossing angle may be adequate. It was nevertheless agreed to negotiate for a higher low beta value of $\beta^* = 2.0$ m for LHCb in IR8 to guarantee realistic operational conditions. The pessimistic data for the extreme case are used to fix the tolerances in IR2 and IR8 only. Otherwise, the aperture would be poor in IR1 and IR5, see sub-plots 52 and 62 in Figure 8. In nominal conditions (full beam intensity), β^* is larger in IR2 and IR8 and the case 'PRE-COLLISION NOMINAL' applies for IR1 and IR5, see above.

In the experimental insertions, thanks to the presence of both remotely controlled motorized jacks and to on-line survey equipment, the tunnel tolerances can be safely confined to [17]

$$\Delta r_{\rm tunnel} = r_{\rm beam} - r_{\rm WP18} = 0.6 \text{ mm}. \tag{6}$$

The tolerances h and v at WP18 are therefore equal to those for the tunnel, while r is smaller by 0.6 mm at WP18. The tolerances are conservatively set to be constant along Q1/MQXA and Q3/MQXC, even if some relaxation can apply to one extremity in many cases, see Figure 8. In practice, this relaxation did not need to be used up. The data for the different assemblies and insertions are given in Table 9. As for the doublets Q2/MQXB,

Table 8: Optics parameters at the collision points used to fix the geometrical tolerances.

Case	Parameter	Unit	IR1	IR2	IR5	IR8
	Crossing Plane		V	V	H	H
Injection	β^*	[m]	17	10	17	10
	$\alpha_{\rm cross}$	[μrad]	160	170	160	170
Pre-collision	β^*	[m]	0.55	10	0.55	10
Proton Nominal	$\alpha_{\rm cross}$	[μrad]	142.5	170	142.5	210
Pre-collision	β^*	[m]	0.55	0.5	0.55	1.0
Extreme case	$\alpha_{\rm cross}$	[μrad]	142.5	80	142.5	210

Table 9: Racetrack tolerance data for the MQX triplet quadrupoles at the time of fiducialisation WP18. $h_{\rm beam}$ and $v_{\rm beam}$ are equal to $h_{\rm WP18}$ and $v_{\rm WP18}$ respectively.

Element	IR	$h_{\rm WP18}$ [mm]	$v_{\rm WP18}$ [mm]	$r_{0,\rm WP18}$ [mm]	$r_{0,\rm beam}$ [mm]	a [mm $\times$ m^{-2}]	Crossing Plane
MQXA	1,2,5,8	1.0	1.0	0.7	1.3	0	H or V
MQXB	1,2	0.6	0.0	0.3	0.9	3.7 10^{-2}	V
MQXB	5,8	0.0	0.6	0.3	0.9	3.7 10^{-2}	H
MQXC	1	0.8	0.0	0.5	1.1	0	V
MQXC	5	0.0	0.8	0.5	1.1	0	H
MQXC	2,8	1.0	1.0	0.7	1.3	0	H or V

and similarly to arc SSS, with both the beta functions and the crossing-scheme trajectories reaching their maximum in the middle of the assembly, a running radial component $r(y)$ was fitted to the optics data. We get

$$r_{\rm WP18}(y) = r_0 + a(y - y_0)^2 \ , \tag{7}$$

with y_0 being the center of the assembly and with r, r_0 in mm and y, y_0 in m. The quantities r_0 and a are given in Table 9.

9 Cold feed-boxes of the MQX/MBX sections DFBX

Thanks to the choice of a large cold bore in the DFBX (Table 1) which is located between the triplet quadrupole Q3 and the MBX/MBXW separation dipoles, an aperture $n_1 > 8$ is met with rather large tolerances, see Table 10.

Table 10: Tolerance for the DFBX.

Step	h [mm]	v [mm]	r [mm]
Workshop	3.0	3.0	0.0
Tunnel	0.36	0.0	0.84
Beam	3.36	3.0	0.84

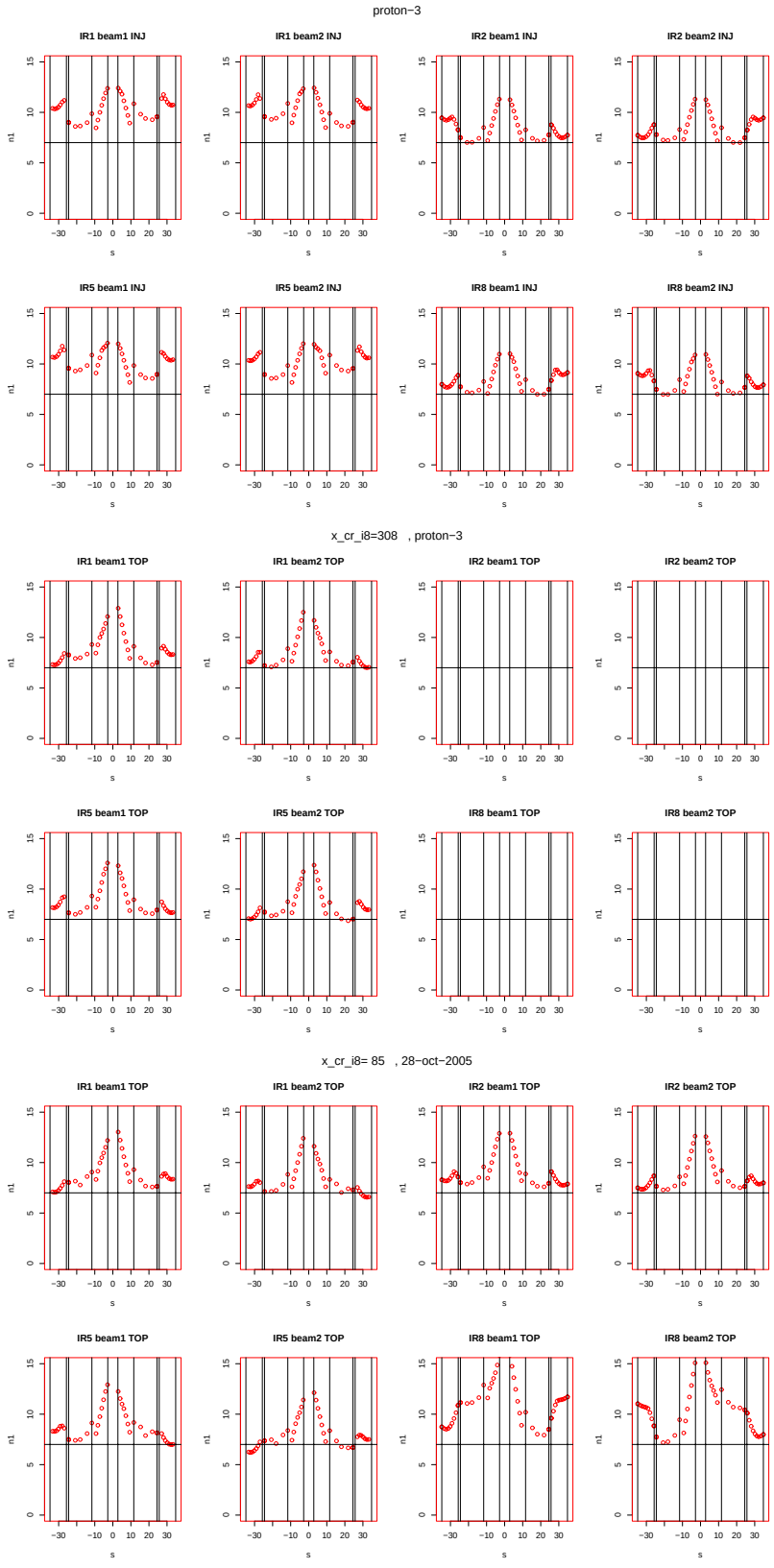

Figure 8: Aperture along the triplets with the tolerances as defined in Table 9. Rows 1 and 2: INJECTION, raws 3 and 4: PRE-COLLISION NOMINAL, rows 5 and 6: WORST CASE. In the text, we refer to a single plot by using a matrix notation : row number followed by column number, example: Beam2 in IR5 for nominal pre-collision: plot 42.

10 Cold separation dipoles, MBX, MBRC, MBRB and MBRS

Cold separation/recombination dipoles(MBRC or D2) are used in IR1, IR2, IR5 and IR8 at the end of the matching sections in order to bend Beam1 and Beam2 such as to point to the collision point. In IR2 and IR8, a cold single bore dipole (MBX) is used to compensate the angle made by D2. In IR4, cold D3 and D4 (MBRS and MBRB, respectively) are used to form a dogleg which separates the two beams from 194 to 420 mm in order to provide transverse space to the RF cavities. All these magnets have a straight cold mass, with the cold bore axis made parallel to the central axis, while each beam is bent towards or away from the central axis. MadX computes physical quantities around the beam trajectory. It is thus blind to the transverse offset w.r.t. the cold bore axis. Aperture calculations therefore requires to use *offset files* which describe the running horizontal offset inside these dipoles, as follows :

```
select,flag=aperture,column=name,s,n1,betx,bety,dx,dy,x,y;
aperture, range=e.DS.L1.B1/s.DS.R1.B1, cor=0.004, spec=7, interval=1.0,
offsetelem="offset_ir1_b1",file="ap.ir1.b1";
```

The offset files for each beam and each IR are stored in

```
/afs/cern.ch/eng/lhc/aperture/ref_data/offset_files
```

10.1 MBX, MBRC

Both MBX (D1) and MBRC (D2) in IR1, IR5, IR2R and IR8L are quite easy and tolerances can be quite large while keeping $n_1 > 7$, see Table 11. As for IR2L and IR8R (D2L2, D2R8 or MBRC.L2, MBRC.R8), where Beam1 and Beam2 are respectively injected, the case is more difficult. MKI errors may kick some beam or halo well above the nominal beam axis [18]. The situation is most critical on the IP side of D2, where the tolerance is close to zero in the vertical plane, see Table 11. The h and v-tolerance along the magnet must be linearly interpolated between the values quotes on the IP-side and on the Non-IP-side, see also Section 14.3 for aperture data. These restricted tolerances apply to the aperture of the injected beam, while to the non-injecting aperture the tolerances of the more easy D2 cases listed in Table 11 are applied. The case of aperture with MKI error is further discussed considering the measured assemblies in Section 14.3.

10.2 MBRB, MBRS

The MBRS (D3) dipoles, which delimit the central part of IR4beam with enlarged beam separation are quite easy, because of moderately large β-functions, see [19, 20]. With the quoted tolerances which correspond to the measured profiles, we get $n_{1,\min} = 8$. The MBRB (D4) is more difficult. With the beam entering the magnet from the dispersion suppressor at the nominal $x_1 = 97$ mm distance from the central axis, and being bent away along the dipole by 7.4 mm, it emerges on the IP-side of the MBRB at $x_2 = 104.4$ mm. The design interbeam distance was therefore set to be twice the average of these two values, namely $d = x_1 + x_2 = 202$ mm (rounded). The MBRB were instead built with $d = x_1 + x_2 = 194$ mm. This was partly corrected by curving the cold bore with special

Table 11: Tolerances at WP18 and in the tunnel data after one year of operation for the cold separation/recombination dipoles.

Element	IR/slot	h [mm]	v [mm]	h [mm]	v [mm]	r [mm]
		WP18		Beam		
MBX (D1)	2,8	2.0	2.0	2.36	2.0	0.84
MBRC (D2)	1,5	2.0	2.0	2.36	2.0	0.84
MBRC (D2)	IR2R,IR8L	2.0	2.0	2.36	2.0	0.84
MBRC (D2)	IR2L,IR8R, NIP side	2.0	2.0	2.36	2.0	0.84
MBRC (D2)	IR2L,IR8R, IP side	1.0	0.3	1.36	0.3	0.84
MBRS (D3)	4	1.5	1.2	1.86	1.2	0.84
MBRB (D4)	4	1.0	0.6	1.36	0.6	0.84

supports in the coils, in order to get $d_{\rm IP} = 198.6$ mm. But each aperture is still smaller than the design value by 1.7 mm. The tolerances quoted in Table 11 correspond to the measured profiles and by shifting at best the magnets. The resulting normalised aperture are

$$n_1 = 7.05 \ \text{ for MBRB.L4} \quad \text{and} \quad n_1 = 7.4 \ \text{ for MBRB.R4.} \tag{8}$$

The shifts were set such as to equalize the aperture of Beam1 and Beam2, see [21, 22]. The offset files for each beam are stored in

```
/afs/cern.ch/eng/lhc/aperture/ref_data/offset_files
```

11 Injection and dump septa, MSI and MSD

A detailed discussion of geometry issues and results for both the injection (MSI) and dump septa (MSD) is presented in [23, 24]. Further allocation work was presented at MEB [25, 26]. The geometrical errors are partly integrated into effective vacuum chamber data and partly into errors of positionning w.r.t. the survey target and reference points located on the top of the laminations (tilt control). The vacuum chamber of these elements are made of mu-metal, in order to reduce the magnetic residual field and to save aperture (no space for an additional stainless steel cold bore). They present a slight ovalisation w.r.t. the specified circular shape. In the MSI for IR2 and IR8, where the aperture is more critical, the chamber were sorted with to respect to their rectitude and with the ovalisation oriented at best. The MSD chambers are oriented randomly, and the smallest dimension is used to defined an inscribed circular aperture. Aperture and tolerance data used in MadX are given in Table 12. Tolerances are defined directly for the tunnel, according to Figure 7 and Formulae (2), see Section 6. The aperture calculation proper is made more complicated for both MSI and MSD because of the longitudinaly inclined circulating beam openings (this to allow for a straight line in the injection aperture where aperture is severely limited), see [23, 24]. Aperture calculations with MadX therefore requires to use *offset files* which describe the running vertical offset of MSIs and the horizontal one of MSD, as follows :

```
select,flag=aperture,column=name,s,n1,betx,bety,dx,dy,x,y;
```

Table 12: Aperture and tolerance data for MSI and MSD

Element	IR	h [mm]	v [mm]	h [mm]	v [mm]	r [mm]	aper_1,3 [mm]	aper_2,4 [mm]
		Workshop		Beam				
MSI	2,8	1.0	1.0	1.36	1.0	0.84	28.3	28.7
MSD	6	1.0	1.0	1.36	1.0	0.84	28.3	28.3

```
aperture, range=e.DS.L6.B1/s.DS.R6.B1, cor=0.004, spec=7, interval=1.0,
offsetelem="offset_ir6_b1",file="ap.ir6.b1";
```

The offset files are stored in

```
/afs/cern.ch/eng/lhc/aperture/ref_data/offset_files
```

With the data of Table 12, the minimum of n_1 is for all of the MSIs $n_{1,\min} = 7.7$ and for the MSDs $n_{1,\min} = 7.6$.

12 Warm magnets in IR3 and IR7

The central section of IR3 and IR7 is made of warm magnets. Each extremity is occupied by a dog-leg section built-up with MBW dipoles which have a common gap for both beam apertures. The central section is occupied by 4 assemblies of six MQW quadrupoles, each assembly being followed, or preceeded, by an orbit corrector MCBWH or MCBWV.

12.1 MBW and MCBW

The data for both aperture (elliptical chambers) and tolerances are given in Table 13. The vacuum chamber of MCBW was chosen to be identical to the one of MBW, instead of the one installed in MQW in order to overcome a severe aperture in some of these. Tolerances are here computed from measured chambers (inner size, h and v rectitudes), magnet geometry (twist, yoke-to-target error) and chamber positionning w.r.t. to yoke reference [27]. The smallest measured chamber data are used, with all chambers measured. Limited sorting was made. Detailed input data and results can be found in [28]. Few points must be noted

- The aperture calculation in MBW with Madx requires the use of offset-files, see Section 11. The four offset-files can be found at

  ```
  /afs/cern.ch/eng/lhc/aperture/ref_data/offset_files
  ```

- For space considerations, the passive chamber alongside the MBCWs has the same shape than inside the MCBW. Both were treated identically. No entry exists as of today in the LHC sequence. An addition is made to the sequence, see the 'VIRTM-CBW' seqedit in the MadX script

  ```
  /afs/cern.ch/eng/lhc/aperture/ref_data/final.ap.tol.2007.forseq/dpir37.b1.madx
  ```

Table 13: Aperture and tolerance (tunnel) data for MBW and MCBW

Element	IR	h [mm]	v [mm]	h [mm]	v [mm]	r [mm]	aper_1,3 [mm]	aper_2,4 [mm]
		Workshop		Tunnel				
MBW	3,7	1.7	1.4	2.1	1.4	0.84	29.4	22.1
MCBWH	3,7	1.3	1.65	1.7	1.65	0.84	29.4	22.1
MCBWV	3,7	1.7	1.7	2.1	1.7	0.84	22.1	29.4

With the quoted tolerances, the normalised minimum aperture is $n_{1,\min} = 7.4$ in MBWs and $n_{1,\min} = 8.2$ in MCBWs.

12.2 MQW

For historical reasons (late decision to insert a bake-out system around the vacuum chamber, yoke which could not be assembled in the presence of the vacuum chamber), the aperture is critical in the MQW magnets. We therefore sorted both the yokes and the vacuum chambers, such as to maximimize the aperture. The one-by-one tolerances are determined in a way which is similar to the one used for MBW , see Section 12.1. Input data can be found in [29]. The most difficult aperture/slots were granted the best yokes and the best chambers (largest inner size and best rectitude in the critical plane), but making some compromize with the sorting of the transfer functions in order to reduce the β-beating. Then, iteratively, the other slots are filled with the same criteria. A detailed table of slot filling with yokes and chambers can be found in [30]. As a result, generic tolerances cannot be used for the MQW-class in MadX. Rather, the one-by-one slot data are added to the sequence. The complete files is

`/afs/cern.ch/eng/lhc/aperture/ref_data/final.ap.tol.2007.forseq/tolapmqwseq.new2007`

with a few lines given here below

```
MQWA.E5L3.B1,APERTYPE=RECTELLIPSE,APERTURE={0.01547,0.02600,0.01547,0.02600};
MQWA.E5L3.B2,APERTYPE=RECTELLIPSE,APERTURE={0.02612,0.01525,0.02612,0.01525};
MQWA.E5L3.B1,APER_TOL={ 0.00084, 0.00044, 0.00021};
MQWA.E5L3.B2,APER_TOL={ 0.00084, 0.00044, 0.00021};
...
MQWA.E5R7.B1,APERTYPE=RECTELLIPSE,APERTURE={0.02603,0.01527,0.02603,0.01527};
MQWA.E5R7.B2,APERTYPE=RECTELLIPSE,APERTURE={0.01529,0.02610,0.01529,0.02610};
MQWA.E5R7.B1,APER_TOL={0.00084,0.00044,0.00019};
MQWA.E5R7.B2,APER_TOL={0.00084,0.00044,0.00019};
```

After sorting, the minimum of aperture in MQW is $n_{1,\min} = 6.0$ in IR3 and $n_{1,\min} = 6.5$ in IR7.

12.3 Aperture treatment in IR3

The aperture calculation in the presence of momentum collimation requires a special treatment. The primary collimators of IR3 are set to cut the halo in δp. But the β

functions cannot be vanished, and therefore the halo is cut in a correlated way between longitudinal and transverse amplitudes. The formalism is described in [31], see also [2] and [30]. With MadX, the aperture command must include the bucket *dp* width and the corresponding limited halo size, as follows

```
select,flag=aperture,column=name,n1,rtol,xtol,ytol,
aper_1,aper_2,aper_3,aper_4,betx,bety,dx,dy,x,y;
aperture,range=e.DS.L3.B1/s.DS.R3.B1,cor=0.004, spec=7, interval=1.0,
file="ap.ir3.b1",halo={ 6.0, 8.4, 4.97, 7.2},dp= 0.001500;
plot,table=aperture,noline, haxis=s,vaxis=on_elem, n1,spec,vmin=0,vmax=12,
colour=100,title="n1 IR3 Beam1",file="plot.dp.b1";
```

This command is extracted from the above-mentioned file

```
/afs/cern.ch/eng/lhc/aperture/ref_data/final.ap.tol.2007.forseq/dpir37.b1.madx
```

This way of computing applies to IR3 from Q13L to Q13R only. In case the momentum cleaning is not used, the large dipersion in IR3 will be suppressed in order to make the aperture large in this section. But of course, in this case, the cut of the betatronic amplitude with δp disappears while the dispersion function remains as in the rest of the ring.

13 Warm separation dipoles in IR1 and IR5, MBXW

The warm separation dipoles MBXW in IR1 and IR5 have a small vertical gap and a large horizontal aperture. They are equipped with large and flat vacuum chamber of half inner dimensions

$$a = 64 \text{ mm} \text{ and } b = 26.5 \text{ mm} \tag{9}$$

The one-by-one tolerances are determined in a way which is similar to the one used for MBW in, see Section 12.1. Input data can be found in [32]. The flatness of the ellipse make its difficult to get straight chambers, and they are not constrained horizontally in the wide magnet opening. We therefore made a partial sorting, in order to get a good aperture in some critical slots, namely on the Q3 side in IR1 (vertical crossing plane). We also housed bad chambers in the central MBXW slots of IR5, where aperture is the least critical. This way, all the bad chambers have a negligible impact, and we could keep good spare chambrers, see [33] for detailed data and choices. Tolerances families and their corresponding slots are listed in Table 14.

14 Difficult cases

The aperture in few elements is smaller than the specified n_1 value. All the elements with $n_1 < 7$ in their focussing aperture or $n_1 < 6.7$ in their de-focussing aperture (condition Eq. 1) are listed in Table 15, adapted from [34].

14.1 Dispersion suppressors of IR3 and IR7

In IR3, the aperture is more critical for Beam 2 than for Beam 1 in the dispersion suppressors. The average n_1 are 7.45 and 7.18 for Beam 1 and Beam 2 respectively (aver-

Table 14: Tolerance class data for MBXW at sorting and in the tunnel

Classes	h [mm]	v [mm]	h [mm]	v [mm]	r [mm]	Slots
	Workshop		Tunnel			
Golden	1.0	0.3	1.4	0.3	0.84	A4L1,B4L1,A4R1,B4R1
Bad-h	5.5	0.8	5.9	0.8	0.84	C4R1,D4R1
Bad-v	2.0	1.9	2.4	1.9	0.84	C4L5,D4L5,C4R5,D4R5
Standard	2.5	0.9	2.9	0.9	0.84	everywhere else

aged difference 0.25). The averaged difference amounts to 0.35 for the four elements with worst aperture. A small part of the difference can be explained by the not exactly anti-symmetric layout of the suppressors, but the rest is related to a non-optimised matching of Beam 2. Presently (with sequence V6.5), two elements (Q8L3 and Q9R3) offer $n_1 = 6.2$ and $n_1 = 6.3$ with $h = 0.9$ mm.

14.2 Q6 in IR2 and IR8

The late integration of the DFB at the quadrupole Q7 imposed a move of the quadrupole Q6 in both IR2 and IR8, which was earlier located at best to optimize the phase advance between the injection kicker and a TCLI collimator which supplements the TDI. This move resulted in larger β-functions in these assemblies. The measured assemblies proved to be quite good for Q6L2 and Q6L8 and Q6R8, see Table 15. But Q6R2 remains difficult with $n_1 = 6.7$ in the horizontal plane. With $\beta_{\mathrm{x}} = 400$ m, the missing space is $\Delta x = 0.70$ mm. This can be recovered by correcting the closed orbit locally if necessary, remembering that a closed orbit budget of $\mathrm{CO}_{\mathrm{radial}} = 4$ mm is used by default in all aperture calculations at injection.

14.3 Neighbours of injection kickers

The case of injection errors is discussed for the D2L2 and D2R8 in Section 10.1. Similar conditions apply to Q4L2 and Q5L2 (Beam 1) in IR2 and Q4R8 and Q5R8 (Beam 2) in IR8. The available aperture is given in Table 16. The vertical excursion of the injected beam is large on the MSI side of Q5L2 and Q5R8 at every batch injection. This is a regular case, and the normalised beam shape is round. The same excursion occurs on the D2 side of Q4L2 and Q4R8 only in case of MKI failure, in which case a round beam must be considered. The results for these two cases are listed in Table 16. The case of a kick applied to the circulating beam requires the use of a beam with halo. Two sub-cases must be considered. An asynchronized kick will deflect a full circulating beam in Q4 and D2, in which case with $n_1 > 5$ a quench may occur, but damage is avoided. The other sub-case is related to off-bucket protons which may drift in the time-slot of another batch. A δ_p-dependent fraction of these protons will systematically be deflected at each sub-sequent batch injection [36]. This latter case is further discussed in Section 14.3.1. It is worth noting that in IR8, where the beam-beam crossing scheme is horizontal, the freedom to choose the sign of the parallel separation can be used to minimize these losses by further increasing the aperture for this case, at the detriment of the rare accidental case of non-firing of the MKI. Low β_z-functions (< 70 m) explain the good n_1 value at Q4. At Q5, the case is less good ($\beta_z \simeq 200$ m), even if the beams must be scraped to

Table 15: SSS and SpSSS with a normalised aperture expressed in n_1 units which does not satisfy the specification. Bold data when $n_1 < n_{1,\text{spec}} - 0.1$. All these data obtained with the measured assemblies.

Slot	Element number	$n1$					
			V1		V2		
			F	D	F	D	
Q5L1	620	*beam2*	-	-	**6.8**	-	*beam1*
Q7L2	690	*beam1*	-	-	-	**6.55**	*beam2*
Q10L2	665	*beam1*	-	-	6.9	-	*beam2*
Q6R2	674	*beam2*	**6.70**	-	-	-	*beam1*
Q10R2	678	*beam2*	-	6.66	-	-	*beam1*
Q8L3	520	*beam2*	-	**6.36**	-	-	*beam1*
Q10L3	510	*beam2*	-	**6.67**	-	-	*beam1*
Q9R3	514	*beam2*	-	**6.22**	-	-	*beam1*
Q11R3	525	*beam2*	-	**6.53**	-	-	*beam1*
Q10R4	626	*beam2*	-	6.60	-	-	*beam1*
Q11L5	528	*beam2*	-	-	-	**6.56**	*beam1*
Q10L7	516	*beam1*	-	-	-	**6.58**	*beam2*
Q10R7	504	*beam1*	-	6.60	-	-	*beam2*
Q11R7	508	*beam1*	**6.60**	-	-	-	*beam2*
Q9L8	613	*beam1*	-	-	-	6.60	*beam2*
Q6R8	610	*beam2*	6.90	-	-	-	*beam1*

Table 16: Aperture in elements subject to beam excursion following injection kicker errors, for two cases of closed orbit. The case *round beam* applies to the injected beam, while *beam with halo* applies to a kicked circulating beam.

Element number	n_1, round beam		n_1, beam with halo	
Radial Closed orbit	CO=2	CO=4	CO=2	CO=4
Q5L2	10.0	7.7	-	-
Q4L2	10.8	8.3	8.2	6.3
D2L2	9.2	6.4	6.7	4.6
Q5R8	8.2	5.3	-	-
Q4R8	10.9	8.5	7.9	6.0
D2R8	9.8	7.0	7.0	5.0

$n_1 = 3 - 4\ \sigma$ in the SPS before their transfer, and again at the entrance of the MSI. The values quoted here are obtained with the nominal closed orbit budget of $\mathrm{CO}_{\mathrm{radial}} = 4$ mm and also with $\mathrm{CO}_{\mathrm{radial}} = 2$ mm because the injection channel through the MSIs requires this improved value. If the latter value is indeed reached at the end of the transfer line, a good matching with the circulating beam, which is mandatory to avoid large injection oscillations, would ensure a good aperture with $n_1 \simeq 7$ in IR2. In IR8, a similar result id obtained by applying a longitudinal pitch to Q5R8, such as to lower its MSI-extremity by 1mm, because of the beam entering the ring from below, while keeping in place the integrated transverse magnetic axis of the MQY. A modified fiducialisation file has been prepared by the survey team. The corresponding re-alignment must be performed in the tunnel before commissioning intense beams.

14.3.1 Off-bucket protons and further batch injections

Protons which were injected out of RF buckets or which left their bucket before a further batch is injected creep along the captured bunches. Their creeping speed is steeply dependent on their momentum offset relatively to the bucket width. By integrating the longitunal motion w.r.t. $\delta_1 = \delta_p - \delta_b$, we get $v_{\mathrm{creep}}(\delta_1 = 1.e-5) = -40$ m/s and $v_{\mathrm{creep}}(\delta_1 = 1.e-4) = -60$ m/s. With $\delta_1 > 0$, the protons recess w.r.t. circulating beam, i.e. migrate in the time slot of the next batch to be injected. Depending on the injection scheme (one ring after the other, or one batch per ring), the time spent between two batch injections in one ring is $T = 20$ or $T = 40$ s. With a batch length of $L = 1800$m, the critical speed range to invade the injection gap is $v_c = L/T = 90$ or 45 m/s. These values are very close to above quoted v_{creep}. We shall therefore consider that all of the off-momentum protons will be kicked by the next injected batch.

These protons will be fully kicked and either be directed to the TDI, or for a fraction of them scraping will occur at the extremity of D2 which is away of the MKI. With the aperture in D2 decreasing by 0.8mm per meter and reaching a minimum at its extremity, most of the scaping protons will impact at the latter location. Considering the worst case of the proton shower to be fully absorbed in the coil of D2, the quench limit to consider is $\Delta N = 10^9$ p/m while a batch intensity is $N_b = 2.4\ 10^{13}$. With a minimum aperture $n = 6.4\sigma$ at D2L2 (columns 2 and 3 of Table 16), a quench will occur if the fraction of protons which are both out of bucket and with a betatronic amplitude $A_\beta > n$ is

$$f_{\overline{\mathrm{RF}}} \times f_{A_\beta > 6.4} \ > \ \frac{8\Delta N}{N_b} = 3.2\ 10^{-4} \tag{10}$$

with a approximate geometrical factor of eight. If we consider the pessimistic case $f_{\overline{\mathrm{RF}}} = 0.1$, then a quench is avoided if $f_{A_\beta > 6.4} < 3.2\ 10^{-3}$. In practice, a large fraction of the shower will develop oustide the D2 coil (the proton will interact in the beam screen and in the cold bore. With a clearance of ≈ 1 mm between the cold bore and the coil, most of the shower particles will go forward to the TDI. A decent knowledge of the improvement factor would require a detailed FLUKA simulation.

The above quoted quantities for the quench limit are not much worrying. But, in the absence of a better knowledge of i) the routine value of the fraction of protons out-of-bucket just after capture ii) the population of the halo above $A_\beta > 6.4$ built-up in the first 20 or 40 seconds after injection iii) the quench improvement factor (FLUKA simulation), it would advisable to seriously consider using the option of using the damper to excite the parasitic particles behind the last injected batch, in the same way this will

be used to clean the abort gap.

15 Conclusions

We can summarize the aperture map of the LHC ring after the qualification of all the elements as follows.

MB, MQX, D1-D4, MBXW, MBW, MKI, MSI, MKD, MSD, LE, DFB: The condition $n_1 = 7$ is granted for all these elements.

MQ-SSS: The condition $n_{1,\mathrm{QF}} = 7$ and $n_{1,\mathrm{QD}} = 6.7$ is granted with only a few cases where $\delta n_1 \simeq 0.1$ is missing.

SpSSS: Most of these elements satisfy the condition $n_{1,\mathrm{QF}} = 7$ and $n_{1,\mathrm{QD}} = 6.7$, see below for exceptions.

MQ-SpSSS in IR3 Beam 2: Four elements in the dispersion suppressors of IR3 for Beam 2 exhibit a poor n_1, see Section 14 and Table 15. The matching of Beam 2 is less good than for Beam 1. Additional matching work must be worked-out before revisiting this case. A study is underway to improve this [35].

Isolated difficult MQ-SpSSS: Six isolated assemblies are missing aperture by $\delta n_1 \leq 0.4$. This translates in missing transverse space of either $\Delta x, z \leq 0.7$ mm. This implies that the closed orbit must be locally corrected to better than $CO = 4$ mm by $\Delta x, z$ in the corresponding plane.

SpSSS and D magnets at injection points: This case is discussed in Section 14.3. A dedicated effort in order to reach a closed orbit excursion inside $\mathrm{CO}_{\mathrm{radial}} = 2$ mm in these areas will be much rewarding. Exciting the off-momentum halo behind injected batches shall be considered as well.

MQW: A fraction of the MQW modules exhibit $n_1 = 6.0$ in IR3 and $n_1 = 6.5$ in IR7. Detailed beam loss studies have shown that this is harmless for these elements with the foreseen active and passive protections. Nevertheless, a special care must be devoted to the closed orbit reduction in these areas.

Acknowledgements

This summary of aperture tolerances represents only a small part of the activity which was devoted to the geometry and stability of the magnet assemblies. It was made possible thanks to the clever work of magnet designers and builders. M. Bajko, M. Modena, V. Parma, J.C. Pereira Lopez, K. M. Schirm, F. Seyvet and D. Tommasini from AT/MCS were heavily involved in order to get a good geometry for the main dipole and the main quadrupole assemblies. The geometry of the Special SSS and low-β quadrupoles was worked out by N. Catalan, R. Ostojic, H. Prin and J.C. Perez from AT/MEL. The warm magnet activity was driven by S. Ramberger from AT/MEL. The overall qualification process would not have possible without a systematic and precise infrastructure of measurement of all the assemblies. We are heavily indebted with our collegues of TS/SU, with a special mark to P. Bestmann, D. Missiaen and M. Dupont. All the geometry issues of the beam screen were solved with N. Kos, P. Cruikshank, P. Lepeule and R. Veness from AT/VAC. The vacuum system of the warm magnets was designed by C. Rathjen who implemented clever and innovative features, rescuing the aperture from unforeseen magnet design changes. Combined magnetic and geometric data could be used for the cold qaudrupoles thanks to M. Buzio, S. Pauletta and J. Garcia Perez from AT/MTM. The treatment of the geometry of the injection and dump elements was made by M. Gyr and B. Goddard form AB/BT. An efficient storage and retrieval of the fiducialisation data in Oracle was ensured by J. Beauquis, G. Bevillard, N. Emelianenko and E. Wildner from AT/MCS. Much help was granted by the members of the WGA Working Group and the Magnet Evaluation Board. It is a pleasure to thank of all of them for what revealed to be a many years long and complicated activity. The geometry and aperture work was made in close collaboration with my colleagues from AB/ABP who dealt each with all the other issues of one species of magnet, namely S. Fartoukh, S. Gilardoni, M. Giovannozzi, A. Lombardi, Y. Papaphillipou and F. Schmidt, with a special mark to Stephane who coordinated the LHC magnet activity in our group and who boosted the qualification and sorting activities at the project level. Finally, I wish to thank Marta once more, for being involved in the geometry of the cold magnets from the early days and who initiated and implemented the geometry measurements in the industry. She disclosed and solved many issues related to not always coherent specifications and inevitable surprises during the early days of production. Her help in the management of the WGA Working Group is invaluable.

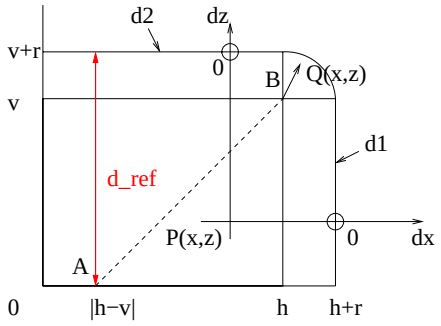

Figure 9: Race-track and distance definition.

16 Appendix A : Race-track distance: definition and algorithm

In order to check the quality of the profile of a magnet with respect to a racetrack tolerance definition, a race-track distance $d_{\rm rt}$ must be defined in order to quantify the transverse position of a point $\mathbf{P}(x,z)$ with respect to the edge of the boudary of the racetrack given by its three parameters h, v, r. This distance must be

1. metric
2. $d_{\rm rt} \geq 0$
3. compared to a reference distance $d_{\rm ref}$ which is constant whatever the location of the point $\mathbf{P}(x,z)$ to be checked

By inspecting Figure 9, we see that the largest possible shortest distance to the edge of the race-track is $d_{\rm ref} = \min(h,v)+r$. This quantity will be the reference distance, see item 3 above. Then, the race-track distance of the points which are located along the segment **OA** must be $d_{\rm rt} = 0$. And as well, the race-track distance of the points which are located on the lines d_1 and d_2 must be the $d_{\rm rt} = d_{\rm ref}$. Leaving apart the points which are located in or beyond the upper-right quarter circle, these conditions are satisfied by computing the signed shortest distance of $\mathbf{P}(x,y)$ to d_1 and d_2, or respectively

$$dx = x - (h+r) \quad , \quad dz = z - (v+r) \ , \tag{11}$$

then by adding $d_{\rm ref}$ to the largest of these two values (they are signed and negative if $P(x,z)$ is inside the race-track). The race-track distance is then

$$d_{\rm rt} = \max(dx,dz) + d_{\rm ref} = \max(x-(h+r), z-(v+r)) \ + \ \min(h,v)+r \ \text{ if x < h or z < v .} \tag{12}$$

As for the upper-right quarter circle, adding $\min(h,v)$ to $||\mathbf{BQ}||$ is coherent with the above (If $\mathbf{Q}$ is on the circle circumference, we get $d_{\rm rt} = \min(h,v) + r = d_{\rm ref}$). It follows

$$d_{\rm rt} = \sqrt{(x-h)^2 + (z-v)^2} \ + \ \min(h,v) \ \text{ if x > h and z > v .} \tag{13}$$

The following piece of code allows to compute the race-track distance $d_{\rm rt}$ of a point $\mathbf{P}(x,z)$ for a race-track set of parameters (h,v,r):

```
def get_drt(x,z,h,v,r):
    if x>=h and z>=v :
       drt = sqrt((x-h)**2+(z-v)**2) + min(h,v)
    else :
       drt = max( x-(h+r),z-(v+r) ) + min(h,v) + r
    return drt
```

References

[1] http://lhc.web.cern.ch/lhc/, then 'publications'.
[2] LHC Design Report, CERN-2004-003 Volume I, June 2004.
[3] I.K. Waarum, Computation of accelerator aperture and its application to LHC, Sør-Trøndelag Univ. College, 2004 and APERTURE command in MadX home page.
[4] H. Grote and F. Schmidt, The MadX code, see at http://mad.home.cern.ch/mad/
[5] M. Dupont, D. Missiaen and L. Peguiron, Proc. 6th International Accelerator Alignment Workshop IWAA99, Grenoble 1999 and CERN EDMS 107459.
[6] V. Baglin and N. Kos, Beam screens for the long straight sections, Functional Specification LHC-VSS-ES-0002 rev 1.2, edms doc 334961, october 2004.
[7] J.B. Jeanneret, Beam screens in the DFBA's, DFBX's and in Q7, Engineering Change Request LHC-VSS-EC-0008, edms doc 483868, July 2004.
[8] J.P. Quesnel, Minutes of the 9th Parameter and Layout Committee, October 1996.
[9] M. Bajko, J.B. Jeanneret, D. Missiaen, V. Parma, A. Poncet, W. Scandale, and D. Tommasini, LHC Project Note 340, March 2004.
[10] S. Fartoukh, J.B. Jeanneret, J.P. Quesnel and D. Missiaen, Aperture tolerances at WP08 and ITP20 (Main Dipole), Minutes of the WGA55, December 2003, http://lhc-proj-wga-wgr.web.cern.ch/lhc-proj-wga-wgr/default.htm.
[11] J.B. Jeanneret, Minutes of the 43rd Parameter and Layout Committee, October 1998.
[12] S. Fartoukh, Proc. of the XIII CERN-AB Chamonix Wshop, p.148, February 2004.
[13] S. Fartoukh, Proc. of EPAC 2004, Luzern, and LHC Report 769, July 2004.
[14] J.B. Jeanneret, Geometrical tolerances of Arc SSS, March 2005,WGA site, http://lhc-proj-wga-wgr.web.cern.ch/lhc-proj-wga-wgr/default.htm.
[15] The LHC sequence V6.5, March 2004.
[16] J.B. Jeanneret, Minutes of the 153th MEB meeting, February 2007.
[17] J.B. Jeanneret, Minutes of the 101st MEB meeting, November 2005.
[18] J.B. Jeanneret, Minutes of the 65th LTC meeting, November 2006.
[19] J.B. Jeanneret, Minutes of the 123th MEB meeting, May 2006.
[20] J.B. Jeanneret, Minutes of the 138th MEB meeting, September 2006.
[21] J.B. Jeanneret, Minutes of the 129th MEB meeting, July 2006.
[22] J.B. Jeanneret, Minutes of the 136th MEB meeting, September 2006.
[23] B. Goddard et al., Strategy for allocating the MSI magnets and vacuum chambers, LHC Project Note 387, February 2006.
[24] B. Goddard et al., Strategy for allocating the MSD magnets and vacuum chambers, LHC Project Note 388, October 2006.
[25] S. Ramberger, Minutes of the 117th MEB meeting, March 2005.
[26] J.B. Jeanneret and M. Giovannozzi, Minutes of the 144st MEB meeting, Nov. 2006.
[27] S. Ramberger, Minutes of the 135th MEB meeting, September 2006.
[28] J.B. Jeanneret, Minutes of the 138th MEB meeting, September 2006.
[29] S. Ramberger, Minutes of the 128th MEB meeting, July 2006.
[30] J.B. Jeanneret, Minutes of the 129th MEB meeting, June 2006.
[31] J.B. Jeanneret, Phys. Rev. ST-AB **1** 081001, December 1998.
[32] S. Ramberger, Minutes of the 119th MEB meeting, April 2006.
[33] J.B. Jeanneret, Minutes of the 119th MEB meeting, April 2006.
[34] M. Giovannozzi, private communication, March 2007.
[35] M. Giovannozzi and T. Risselada, private communication, March 2007.
[36] S. Fartoukh,65th CERN-LTC committee, 22nd November 2006.